Research Article | Vol. 26, No. 11 | 28 May 2018 | OPTICS EXPRESS 14719
Optics EXPRESS

Complete reconstruction of ultra-broadband isolated attosecond pulses including partial averaging over the angular distribution

THOMAS GAUMNITZ, AROHI JAIN, AND HANS JAKOB WÖRNER*

Laboratorium für Physikalische Chemie, ETH Zürich, Vladimir-Prelog-Weg 2, 8093 Zürich, Switzerland
*hwoerner@ethz.ch

Abstract: Attosecond streaking is a powerful tool to investigate ultrafast electron dynamics on the attosecond time scale. To obtain the highest temporal resolution in a pump-probe experiment, soft-X-ray (SXR) and infrared (IR) pulses have to be carefully characterized. Here, we present a detailed description of our recent generalization of the Volkov-transform generalized projection algorithm (VTGPA) and its application to multiple overlapping photoelectron bands. This method allows for the complete temporal reconstruction of both IR and SXR pulses under the inclusion of accurate complex photoionization matrix elements (PMEs). In this article, we compare the performance of our new method with traditional algorithms. We particularly focus on the important role played by the photoelectron angular distribution (PAD) which needs to be taken into account for the highest fidelity of attosecond pulse reconstruction. For this purpose, we investigate numerically the influence of the finite collection angle of the electron spectrometer on the retrieval and the obtained pulse parameters. We further theoretically demonstrate the reliability of the reconstruction for pulse durations even shorter than the atomic unit of time.

OCIS codes: (320.7100) Ultrafast measurements; (140.7240) UV, EUV, and X-ray lasers; (320.6629) Supercontinuum generation.

References and links

1. M. Drescher, M. Hentschel, R. Kienberger, M. Uiberacker, V. Yakovlev, A. Scrinzi, T. Westerwalbesloh, U. Kleineberg, U. Heinzmann, and F. Krausz, "Time-resolved atomic inner-shell spectroscopy," Nature **419**, 803–807 (2002).
2. A. L. Cavalieri, N. Müller, T. Uphues, V. S. Yakovlev, A. Baltuška, B. Horvath, B. Schmidt, L. Blümel, R. Holzwarth, S. Hendel, M. Drescher, U. Kleineberg, P. M. Echenique, R. Kienberger, F. Krausz, and U. Heinzmann, "Attosecond spectroscopy in condensed matter," Nature **449**, 1029–1032 (2007).
3. P. Eckle, A. N. Pfeiffer, C. Cirelli, A. Staudte, R. Dorner, H. G. Muller, M. Buttiker, and U. Keller, "Attosecond Ionization and Tunneling Delay Time Measurements in Helium," Science **322**, 1525–1529 (2008).
4. G. Sansone, F. Kelkensberg, J. F. Pérez-Torres, F. Morales, M. F. Kling, W. Siu, O. Ghafur, P. Johnsson, M. Swoboda, E. Benedetti, F. Ferrari, F. Lépine, J. L. Sanz-Vicario, S. Zherebtsov, I. Znakovskaya, A. L'Huillier, M. Y. Ivanov, M. Nisoli, F. Martín, and M. J. J. Vrakking, "Electron localization following attosecond molecular photoionization," Nature **465**, 763–766 (2010).
5. F. Calegari, D. Ayuso, A. Trabattoni, L. Belshaw, S. De Camillis, S. Anumula, F. Frassetto, L. Poletto, A. Palacios, P. Decleva, J. B. Greenwood, F. Martin, and M. Nisoli, "Ultrafast electron dynamics in phenylalanine initiated by attosecond pulses," Science **346**, 336–339 (2014).
6. P. M. Kraus, B. Mignolet, D. Baykusheva, A. Rupenyan, L. Horny, E. F. Penka, G. Grassi, O. I. Tolstikhin, J. Schneider, F. Jensen, L. B. Madsen, A. D. Bandrauk, F. Remacle, and H. J. Wörner, "Measurement and laser control of attosecond charge migration in ionized iodoacetylene," Science **350**, 790–795 (2015).
7. M. Huppert, I. Jordan, D. Baykusheva, A. von Conta, and H. J. Wörner, "Attosecond Delays in Molecular Photoionization," Phys. Rev. Lett. **117**, 093001 (2016).
8. S. Pabst, M. Lein, and H. J. Wörner, "Preparing attosecond coherences by strong-field ionization," Phys. Rev. A **93**, 023412 (2016).
9. C. Spielmann, "Generation of Coherent X-rays in the Water Window Using 5-Femtosecond Laser Pulses," Science **278**, 661–664 (1997).
10. E. Seres, J. Seres, F. Krausz, and C. Spielmann, "Generation of Coherent Soft-X-Ray Radiation Extending Far Beyond the Titanium L-Edge," Phys. Rev. Lett. **92**, 163002 (2004).
11. E. J. Takahashi, T. Kanai, K. L. Ishikawa, Y. Nabekawa, and K. Midorikawa, "Coherent water window X ray by phase-matched high-order harmonic generation in neutral media," Phys. Rev. Lett. **101**, 1-4 (2008).

#321407 https://doi.org/10.1364/OE.26.014719
Journal © 2018 Received 6 Feb 2018; revised 20 Apr 2018; accepted 24 Apr 2018; published 25 May 2018

Optics EXPRESS

12. T. Popmintchev, M.-C. Chen, D. Popmintchev, P. Arpin, S. Brown, S. Alisauskas, G. Andriukaitis, T. Balciunas, O. D. Mücke, A. Pugzlys, A. Baltuska, B. Shim, S. E. Schrauth, A. Gaeta, C. Hernandez-Garcia, L. Plaja, A. Becker, A. Jaron-Becker, M. M. Murnane, and H. C. Kapteyn, "Bright Coherent Ultrahigh Harmonics in the keV X-ray Regime from Mid-Infrared Femtosecond Lasers," Science **336**, 1287–1291 (2012).
13. S. L. Cousin, F. Silva, S. Teichmann, M. Hemmer, B. Buades, and J. Biegert, "High-flux table-top soft x-ray source driven by sub-2-cycle, CEP stable, 1.85-μm 1-kHz pulses for carbon K-edge spectroscopy," Opt. Lett. **39**, 5383 (2014).
14. Y. Pertot, C. Schmidt, M. Matthews, A. Chauvet, M. Huppert, V. Svoboda, A. von Conta, A. Tehlar, D. Baykusheva, J.-P. Wolf, and H. J. Wörner, "Time-resolved x-ray absorption spectroscopy with a water window high-harmonic source," Science **355**, 264–267 (2017).
15. J. Li, X. Ren, Y. Yin, K. Zhao, A. Chew, Y. Cheng, E. Cunningham, Y. Wang, S. Hu, Y. Wu, M. Chini, and Z. Chang, "53-attosecond X-ray pulses reach the carbon K-edge," Nat. Commun. **8**, 186 (2017).
16. T. Gaumnitz, A. Jain, Y. Pertot, M. Huppert, I. Jordan, F. Ardana-Lamas, and H. J. Wörner, "Streaking of 43-attosecond soft-X-ray pulses generated by a passively CEP-stable mid-infrared driver," Opt. Express **25**, 27506 (2017).
17. J. B. West and G. V. Marr, "The Absolute Photoionization Cross Sections of Helium, Neon, Argon and Krypton in the Extreme Vacuum Ultraviolet Region of the Spectrum," Proc. Royal Soc. A **349**, 397–421 (1976).
18. J. Mauritsson, P. Johnsson, E. Gustafsson, A. L'Huillier, K. J. Schafer, and M. B. Gaarde, "Attosecond Pulse Trains Generated Using Two Color Laser Fields," Phys. Rev. Lett. **97**, 013001 (2006).
19. I. Grguraš, A. R. Maier, C. Behrens, T. Mazza, T. J. Kelly, P. Radcliffe, S. Düsterer, A. K. Kazansky, N. M. Kabachnik, T. Tschentscher, J. T. Costello, M. Meyer, M. C. Hoffmann, H. Schlarb, and A. L. Cavalieri, "Ultrafast X-ray pulse characterization at free-electron lasers," Nat. Photonics **6**, 852–857 (2012).
20. E. P. Månsson, D. Guénot, C. L. Arnold, D. Kroon, S. Kasper, J. M. Dahlström, E. Lindroth, A. S. Kheifets, A. L'huillier, S. L. Sorensen, and M. Gisselbrecht, "Double ionization probed on the attosecond timescale," Nat. Phys. **10**, 207–211 (2014).
21. H. Li, N. G. Kling, T. Gaumnitz, C. Burger, R. Siemering, J. Schötz, Q. Liu, L. Ban, Y. Pertot, J. Wu, A. M. Azzeer, R. de Vivie-Riedle, H. J. Wörner, and M. F. Kling, "Sub-cycle steering of the deprotonation of acetylene by intense few-cycle mid-infrared laser fields," Opt. Express **25**, 14192 (2017).
22. J. Itatani, F. Quéré, G. L. Yudin, M. Y. Ivanov, F. Krausz, and P. B. Corkum, "Attosecond streak camera," Phys. Rev. Lett. **88**, 173903 (2002).
23. M. Kitzler, N. Milosevic, A. Scrinzi, F. Krausz, and T. Brabec, "Quantum Theory of Attosecond XUV Pulse Measurement by Laser Dressed Photoionization," Phys. Rev. Lett. **88**, 173904 (2002).
24. Y. Mairesse and F. Quéré, "Frequency-resolved optical gating for complete reconstruction of attosecond bursts," Phys. Rev. A **71**, 1–4 (2005).
25. J. Gagnon, E. Goulielmakis, and V. Yakovlev, "The accurate FROG characterization of attosecond pulses from streaking measurements," Appl. Phys. B **92**, 25–32 (2008).
26. P. D. Keathley, S. Bhardwaj, J. Moses, G. Laurent, and F. X. Kärtner, "Volkov transform generalized projection algorithm for attosecond pulse characterization," New J. Phys. **18**, 073009 (2016).
27. H. Wei, T. Morishita, and C. D. Lin, "Critical evaluation of attosecond time delays retrieved from photoelectron streaking measurements," Phys. Rev. A **93**, 053412 (2016).
28. M. Chini, S. Gilbertson, S. D. Khan, and Z. Chang, "Characterizing ultrabroadband attosecond lasers," Opt. Express **18**, 13006 (2010).
29. G. Laurent, W. Cao, I. Ben-Itzhak, and C. L. Cocke, "Attosecond pulse characterization," Opt. Express **21**, 16914 (2013).
30. M. Lucchini, M. Brügmann, A. Ludwig, L. Gallmann, U. Keller, and T. Feurer, "Ptychographic reconstruction of attosecond pulses," Opt. Express **23**, 29502–29513 (2015).
31. M. Schultze, M. Fieß, N. Karpowicz, J. Gagnon, M. Korbman, M. Hofstetter, S. Neppl, A. L. Cavalieri, Y. Komninos, T. Mercouris, C. A. Nicolaides, R. Pazourek, S. Nagele, J. Feist, J. Burgdörfer, A. M. Azzeer, R. Ernstorfer, R. Kienberger, U. Kleineberg, E. Goulielmakis, F. Krausz, and V. S. Yakovlev, "Delay in Photoemission," Science **328**, 1658–1662 (2010).
32. A. Kramida, Yu. Ralchenko, J. Reader, and and NIST ASD Team, NIST Atomic Spectra Database (ver. 5.5.1), [Online]. National Institute of Standards and Technology, Gaithersburg, MD. (2017).
33. G. C. King, M. Tronc, F. H. Read, and R. C. Bradford, "An investigation of the structure near the L 2,3 edges of argon, the M 4,5 edges of krypton and the N 4,5 edges of xenon, using electron impact with high resolution," J. Phys. B **10**, 2479–2495 (1977).
34. R. P. Brent, Algorithms for minimization without derivatives (Prentice-Hall, Englewood Cliffs, New Jersey, 1973).
35. J. Burkardt and R. P. Brent, "BRENT, available at http://people.sc.fsu.edu/~jburkardt/cpp_src/brent/brent.html".
36. A. S. Kheifets, "Time delay in valence-shell photoionization of noble-gas atoms," Phys. Rev. A **87**, 1–9 (2013).
37. S. Bhardwaj, S. K. Son, K. H. Hong, C. J. Lai, F. X. Kärtner, and R. Santra, "Recombination-amplitude calculations of noble gases, in both length and acceleration forms, beyond the strong-field approximation," Phys. Rev. A **88**, 1–7 (2013).
38. J. Gagnon, "Attosecond Electron Spectroscopy - Theory and its Applications," Ph.D. thesis, LMU München (2010).
39. S. Bhardwaj, "Modeling generation and characterization of attosecond pulses," Ph.D. thesis, Massachusetts Institute of Technology (2014).

Optics EXPRESS

1. Introduction

The real-time measurement of electronic dynamics in atoms, molecules and solids has provided essential new insights into their fundamental properties [1–7]. To probe the electron dynamics during photoionization [2], Auger decay [1], or charge migration [4–6], which typically occur on the sub-femtosecond to attosecond time scale, attosecond temporal resolution is required. Huge efforts have been made to generate broader continua for shorter attosecond pulses to resolve faster processes or to reach higher cut-off energies in the water window region. Due to the ponderomotive scaling of the high-harmonic generation (HHG) cut-off ($\propto I\lambda^2$), mid-infrared (mid-IR) laser sources are favorable, which has motivated rapid development in optical parametric amplifier (OPA) and optical parametric chirped pulse amplification (OPCPA) systems during the last years. The longer pulse period of mid-IR driven lasers requires carefully synthesized few-cycle pulses to obtain the highest possible temporal resolution, e.g. in pump-probe experiments utilizing strong-field ionization as the pump [8]. Together with shorter (broadband) attosecond SXR pulses new techniques for a fast and reliable reconstruction of the pulse parameters are needed.

With current sources, ultrabroadband spectra [9–13] reaching K-edges of important elements have been demonstrated. Assuming a perfectly compensated attochirp, these ultrabroad spectra support pulses well below the atomic unit of time (24 as). Recently, the first time-resolved experiment has been performed with such sources [14] and attosecond pulses with new record pulse durations of 53 as [15] and 43 as [16] have been synthesized. For an accurate characterization of these pulses, the standard methods of attosecond science are insufficient, such that sophisticated reconstruction methods beyond the present state-of-the-art are required.

With SXR continua from HHG sources, spanning up to 500 eV the choice of target gas for pulse characterization by attosecond streaking becomes an important parameter. While helium presents the advantage of a single photoelectron line, the cross section drops by several orders of magnitude, from 0.45 Mb at 100 eV to 0.004 Mb at 500 eV [17]. To mitigate the deleterious effect of low photon flux of the SXR sources in addition to the low photoionization cross section, several groups have demonstrated streaking with a magnetic-bottle time-of-flight (MB-TOF) spectrometer owing to its high collection efficiency [18–21]. However, the reconstruction requires an extension of the traditional streaking formalism [22–25] that incorporates the effect of the *photoemission-angle-dependent complex transition amplitudes* (I). Alternatively, other target gases with higher cross sections than helium can be used. However, multiple orbitals are then simultaneously ionized leading to *overlapping energy shifted streaking-spectrograms* (II), which differ from each other in the ionization potentials (IPs) of the involved atomic orbitals of the target and the photoionization matrix elements (PMEs).

In this article, we provide a detailed numerical analysis of our recent generalization of the VTGPA method. We discuss details and present further numerical tests of the reconstruction method underlying our recent publication [16]. We present the extension of the mathematical formalism for the VTGPA method [26], making it suitable for streaking traces recorded with MB-TOFs (cf. (I)) and multiple overlapping photoelectron bands (cf. (II)). Using this new approach, the central momentum approximation (CMA) is no longer required, and any target can be used for streaking as long as the complex-valued, energy-dependent PMEs of the target are incorporated and the angle dependence of the complex transition amplitude can be fully accounted for, allowing for complete temporal reconstruction of isolated attosecond pulses.

2. Ultrashort pulse characterization

Typically two types of algorithms are used for the reconstruction of streaking spectrograms: (a) FROG-type algorithms [24] and (b) phase retrieval by omega oscillation filtering (PROOF) [28,29]. For the principle-component generalized projection algorithm (PCGPA), time and energy domain are connected to each other by Fourier transformation, leading to square streaking spectrogram

Optics EXPRESS

of size $N_E \times N_T$, with $N_E = N$ energy steps and $N_T = N$ time steps. The sampling theorem $\delta E \cdot \delta\tau = 2\pi/N$, therefore defines the amount of data points N that are needed for a measurement at a given energy resolution δE and a time step $\delta\tau$. For ultrashort pulses generated by long wavelength drivers, this leads to extremely large streaking spectrograms. Assuming a delay scan range of 20 fs for a few-cycle mid-IR pulse together with a sub-100 as SXR-pulse a step-size of 10 as is needed to fulfill time-energy requirements and thus results in a spectrogram of $4 \cdot 10^6$ data points, making the measurement and reconstruction extremely challenging and time-consuming. With the least-squares generalized projection algorithm (LSGPA) the sampling condition can be relaxed, with factor L that gives the relation between time sampling steps and delay steps in the experiment $\delta t = \delta\tau/L$ [25]. Recently tomographic reconstruction methods, like ptychography [30] have been proposed and tested with narrowband pulses (≤ 10 eV) because they require the CMA, like FROG algorithms. The limitations of CMA have been discussed extensively in [27]. The PROOF method includes the streaking effect, which is the ponderomotive shift of the photoelectrons, assuming a single-photon interaction with the IR field, which is often not sufficient. The PROOF method is more suitable for multi-cycle IR pulses as the stability of the algorithm strongly relies on a frequency analysis of the streaking spectrogram. Therefore, it is also important that besides the SXR photon absorption only one additional IR photon is absorbed or emitted to avoid the analysis of high-order interactions with the IR field, which requires a precise adjustment of the IR intensity in the experiment. Finally, in the original formulation of PROOF, the IR pulse cannot be reconstructed. This decreases the reliability of the reconstruction as it removes one important quantity for the verification of the retrieval result. In the improved PROOF (iPROOF) method, the physics of the photoionization process is included by using the photoionization matrix elements for a more accurate retrieval process, but also lacks the possibility to reconstruct the IR streaking pulse [29].

Recently, the VTGPA has been proven to overcome the limitations of previous attosecond pulse characterization methods. The VTGPA algorithm [26] allows the reconstruction of both the SXR pulse $\tilde{E}_{SXR}(t)$ and streaking IR field $E(t)$ (or its vector potential $A(t)$), without the need of a Fourier transform to be introduced. Overcoming the limitations of the commonly used PCGPA or LSGPA approaches, VTGPA allows reconstruction without any inherent bandwidth limitation due to the central-momentum approximation and incorporates the target-atom dipole-transition matrix elements. Keathley *et al.* [26] have demonstrated the VTGPA for the case of a transition from a single electronic ground state to a single-ionization continuum state with final momentum $\vec{k}$ on the basis of numerical simulations and experimental data in the regime of attosecond pulse trains. Our work is motivated by the work of Keathley et al. [27] and generalizes their approach to multiple photoelectron bands and includes the photoelectron angular distribution. The first experimental application of the generalized VTGPA to isolated attosecond pulses has been reported by Gaumnitz *et al.* [16].

The original implementation of VTGPA is limited to spectrograms consisting of a single photoelectron band. Depending on the SXR center energy the photoelectron spectrum contains contributions from several orbitals in the case of a multi-electron system. The full streaking spectrogram can then be expressed as a sum of probabilities of the individual transitions from different initial electronic shells to single-ionization continua.

The measured spectrogram is the (incoherent) sum of several energy-shifted streaking spectrograms, which differ from one another because of the different PMEs. For narrowband SXR pulses (≤ 5 eV) photoelectron bands can easily be distinguished from each other, however broadband SXR pulses ($\gg 10$ eV) may lead to multiple overlapping bands, as presented in Fig. 1(A) for a $\tau_{SXR} = 420$ as (narrowband) and (B) a $\tau_{SXR} = 42$ as broadband SXR pulse (center photon energy $W_0 = 110$ eV) streaking a few-cycle pulse at $\lambda_c = 650$ nm. In panel (C), the photoelectrons generated using the same short SXR pulse are streaked using a mid-IR pulse centered at $\lambda_c = 1650$ nm. This spectral domain is referred to as "mid-infrared" within the attosecond

Optics EXPRESS

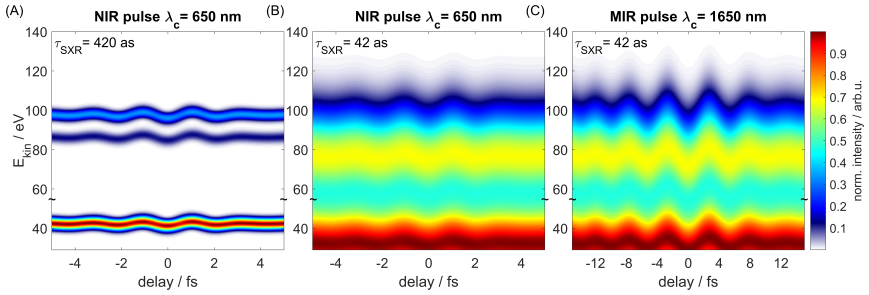

Fig. 1. Simulated traces for a few-cycle near- or mid-IR pulse streaking photoelectrons emitted from xenon by narrow- or broad-band SXR pulses. Panel (A) shows a simulated streaking spectrogram $S(E, \tau)$ for the xenon 5p, 5s, and 4d shells of a few-cycle pulse centered at $\lambda_c = 650\,\text{nm}$ for a $\tau_{SXR} = 420\,\text{as}$ SXR pulse centered at $W_0 = 110\,\text{eV}$. The difference in intensity is due to the included PMEs. The spectrum is sufficiently narrow that the three (5s, 5p, 4d) photoelectron bands are separated from each other. In panel (B) the spectrum of the $\tau_{SXR} = 42\,\text{as}$ pulse is so broad that the individual photoelectron bands from 5p and 5s cannot be separated anymore and a single photoelectron band is observed. The ionization potential of the 4d shell is sufficiently large to be separated from the two other lines, even the wings of the photoelectron lines start to overlap. In panel (C) a mid-IR streaking pulse ($\lambda_c = 1650\,\text{nm}$) with the same intensity was used for comparison with the result in panel (B), where the streaking amplitude has increased due to the longer wavelength of the streaking pulse. All spectrograms are normalized to the peak intensity and plotted on the same false-color representation. The 5s, 5p lines have been scaled by a factor of ≈ 3.3 in intensity, due to the lower cross section.

community, however, the term "short-wavelength infrared (SWIR)" is more widely used. In the latter cases (panel (B) and (C)), the photoelectrons measured at a given energy may originate from different initial electronic shells, which have been ionized to the same final photoelectron energy by different frequencies within the attosecond pulse bandwidth. The individual photoelectron bands cannot be separated anymore and ultrabroadband photoelectron lines are observed. The calculations in Fig. 1 are obtained by evaluating Eq. (1) below, which derives from the strong-field approximation (SFA), which is corrected to include the accurate complex-valued PMEs. This leads to an asymmetric (kinetic-energy dependent) streaking amplitude in the spectrogram for the broadband pulse in panel (B), as the ponderomotive shift Φ of the photoelectrons depends on the initial momentum at ionization $\vec{k}_0$. The effect is more pronounced in panel (C) due to the longer wavelength of the streaking pulse.

For the FROG-type algorithms like LSGPA or PCGPA, that have been used [31], the problem for multiple contributing ionization channels has been solved by assuming a single initial shell. The effect of multiple initial shells is effectively incorporated in the extracted SXR pulse, whose phase depends on both the spectral phase of the SXR pulse and the dipole phase of the initial electronic states. In this article, we provide a detailed numerical analysis of our recent generalization of the VTGPA method for the case of multiple initial states. To exemplify the complete reconstruction of attosecond pulses, including the contribution from several valence orbitals to the photoelectron spectrum, xenon has been used as the target system due to its high cross section, especially for photon energies around 90-100 eV, where most of the streaking experiments have been carried out with Titanium:Sapphire (Ti:Sa) driving laser systems. For long attosecond pulses $\tau_{SXR} \approx 350\,\text{as}$ (bandwidth $\approx 5\,\text{eV}$), the streaking from 5p ($I_{p,5p} \approx 12.1\,\text{eV}$ [32]), 5s ($I_{p,5s} \approx 23.4\,\text{eV}$ [32]), and 4d ($I_{p,4d} \approx 67.5\,\text{eV}$ [33]) channels are well separated and can be reconstructed individually. For shorter pulses with larger bandwidths ($10 - 20\,\text{eV}$) the photoelectron bands start to overlap. In addition, the energy-dependent photoionization matrix elements have to be included into the

Optics EXPRESS

reconstruction method to obtain reliable results, since the cross section of xenon or any other noble gas changes by up to several orders of magnitude over such broad energy ranges, such that their influence cannot be neglected anymore. For even larger bandwidths, photoelectron lines may even overlap completely in the measured spectrogram. Unless a target with contributions from just one single photoelectron line is used, the retrieval algorithm will determine a misleadingly short pulse duration, due to the very large bandwidth "generated" by the coalescence of two individual lines, wherein the retrieval assumes that the bandwidth belongs to a single SXR pulse. To avoid such an erroneous result, all contributing photoelectron lines have to be included with the corresponding PMEs or the measurement has to be performed with helium as the target medium, where the low magnitude of the cross section poses a challenge.

Besides low cross sections and their variation with photon energy (which is typically neglected in PCGPA, LSGPA, PROOF, and related algorithms, except for iPROOF) in the region of interest, the SXR flux might pose a problem for a reliable temporal characterization of the isolated attosecond pulse and the IR pulse. Major issues are the low conversion efficiency of the HHG process in the gas medium, as well as the low reflectivity of the SXR optics, and absorption in metallic filters that are typically used to filter out the residual driving laser and to compensate for the attochirp.

To perform attosecond time-resolved measurements with high stability, with short scan duration, a MB-TOF spectrometer provides an alternative to the traditionally used field-free spectrometers. It increases the collection efficiency and hence the signal-to-noise ratio, by collecting electrons over a finite range of emission angles. This approach allows for faster data acquisition or better statistics.

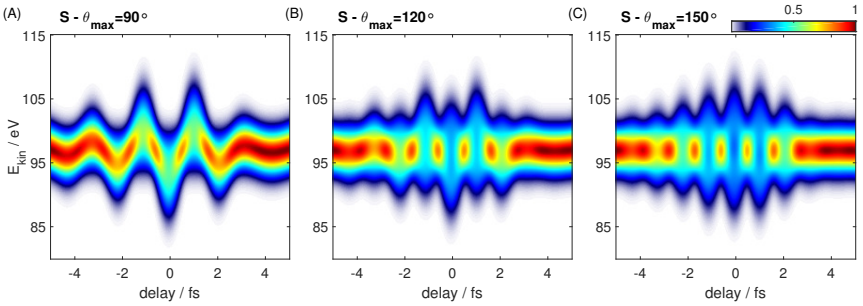

Fig. 2. Simulated streaking traces in helium with a 350 as SXR pulse centered at the photon energy 110 eV for different polar collection angles of the spectrometer. Simulated streaking spectrogram $S(E, \tau)$ in helium for a $\tau_{\mathrm{SXR}} = 350$ as SXR pulse for a spectrometer integrating over a collection polar angle of $\theta_{\mathrm{max}} = 90°$ (A), $\theta_{\mathrm{max}} = 120°$ (B), and $\theta_{\mathrm{max}} = 150°$ (C) normalized on the peak count rate assuming an isotropic photoelectron angular distribution, corresponding to an anisotropy parameter $\beta = 0$.

The overall signal increases, however, the integration of the electrons emitted in different directions by a pulse polarized in the direction of the TOF axis, has to be accounted for in the reconstruction procedure. Figure 2 shows the streaking spectrograms for three different maximum collection polar angles (defined in Fig. 3) of $\theta_{\mathrm{max}} = 90°$ (A), $\theta_{\mathrm{max}} = 120°$ (B), and $\theta_{\mathrm{max}} = 150°$ (C) normalized on the peak count rate assuming an isotropic photoelectron angular distribution, corresponding to an anisotropy parameter $\beta = 0$. So far, several groups have demonstrated streaking using a magnetic-bottle time-of-flight spectrometer, however, the contributions due to collection over a larger finite polar angle has never been accounted for, see e.g. [15, 19]. The simplified streaking formalism, which takes only electrons emitted parallel to the pulse polarization into account, in general fails to reconstruct streaking traces integrated over a finite polar angle. In this article, we discuss the theoretical formalism for streaking taking photoelectron

Optics EXPRESS

angular distributions into account and introduce a retrieval scheme for streaking spectrograms integrated over a large polar angle, due to a large collection angle of the electron spectrometer. We test the method with numerical experiments, using simulated streaking traces. Hereby we show the applicability of this method to attosecond supercontinua of arbitrary bandwidths.

3. Method

The strong-field approximation is commonly used to model photoelectron streaking spectrograms. A linearly polarized attosecond SXR pulse $\vec{E}_{\mathrm{SXR}}(t) = \tilde{E}_{\mathrm{SXR}}(t)e^{iW_0t/\hbar}\vec{e}_{\mathrm{x}}$, where $\tilde{E}_{\mathrm{SXR}}(t)$ is the time-dependent electric-field envelope and W_0 the central photon energy, is assumed to instantaneously promote the transition of an electron from the ground state of a particular shell i of an atom/molecule with the ionization potential $I_{\mathrm{p},i}$ and a PME $d_{(i,\vec{k},\theta)}$ into the continuum with an initial momentum $\vec{k}_0$. During the interaction with the IR streaking field $\vec{E}(t) = E(t)\vec{e}_{\mathrm{x}}$, the momentum $\vec{k}_0$ is modified.

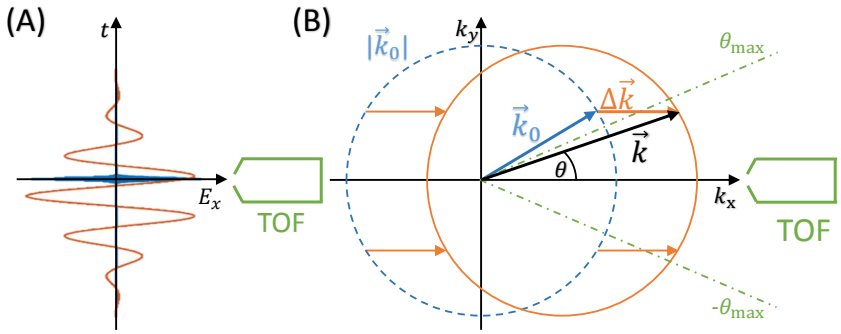

Fig. 3. SXR- and IR-field polarization and the time-of-flight detector. (A) SXR (blue) and IR (red) pulse with linear polarizations, the SXR pulse is described by $\vec{E}_{\mathrm{SXR}}(t) = \tilde{E}_{\mathrm{SXR}}(t)e^{iW_0t/\hbar}\vec{e}_{\mathrm{x}}$, where $\tilde{E}_{\mathrm{SXR}}(t)$ is the time-dependent SXR envelope and W_0 the central photon energy, while the IR streaking pulse is described by $\vec{E}(t) = E(t)\vec{e}_{\mathrm{x}}$. The polarization of both pulses is parallel to the TOF axis. (B) The SXR pulse $\vec{E}_{\mathrm{SXR}}(t)$ leads to photoelectron emission, where $|\vec{k}_0|$ is the absolute value of the initial momentum of the photoelectrons. The angular intensity distribution is included in the PME $d_{(\vec{k}+\vec{A}(t),\theta)} = d_{(\vec{k}_0,\theta)}$. The streaking field $\vec{E}(t)$ changes the momentum by $\Delta\vec{k}$ and the photoelectron with final momentum $\vec{k} = \vec{k}_0 + \Delta\vec{k}$ is detected by the TOF if its angle θ (angle between polarization of the streaking field and the detection direction) is smaller than the maximum photoemission polar acceptance angle $\theta_{\max}$ of the TOF.

Assuming a linearly polarized streaking pulse with the electric field $\vec{E}(t) = -\partial\vec{A}/\partial t$ in the direction of the time-of-flight spectrometer, and the angle θ between the vector potential $\vec{A}$ and the final momentum $\vec{k}$ of a photoelectron (cf. Fig. 3) allows to write the complex transition amplitude $a_i'(|\vec{k}|,\theta,\tau)$ for a transition from the ground state to $|\vec{k}|$ at a particular time delay τ between SXR and IR pulses. This leads to the following equations:

$$\begin{aligned} a_i'(|\vec{k}|,\theta,\tau) &= -i\int_{-\infty}^{\infty} \tilde{E}_{\mathrm{SXR}}(t-\tau)d_{(i,\vec{k}+\vec{A}(t),\theta)}e^{-i\Phi(\vec{k},\theta,t)}e^{i(\vec{k}^2/2+I_{\mathrm{p},i})t}\,\mathrm{d}t \\ \Phi(\vec{k},\theta,t) &= \int_t^{\infty}\left(\vec{k}\cdot\vec{A}(t') + A^2(t')/2\right)\mathrm{d}t'. \end{aligned} \tag{1}$$

The angle-integrated streaking spectrogram $S_i'(|\vec{k}|,\tau)$ for the i-th photoelectron line is then

Optics EXPRESS

calculated by:

$$S_i'(|\vec{k}|,\tau) = \int_{\theta=0}^{\theta_{\max}} \left|a_i'(|\vec{k}|,\theta,\tau)\right|^2 \sin(\theta)\mathrm{d}\theta. \tag{2}$$

A complete streaking spectrogram can be expressed as the sum of individual streaking traces $S_i'(\vec{k},\tau)$:

$$S'(|\vec{k}|,\tau) = \sum_{i=1}^{N_s} S_i'(|\vec{k}|,\tau), \tag{3}$$

where N_s is the number of contributing orbitals (or shells) of the target medium. The merit function M for the least-squares (LS) minimization during the reconstruction routine can be defined as follows:

$$M = \sum_{l=1}^{N_W} \Delta W[l] \sum_{m=1}^{N_\tau} \Delta\tau \left(a'[l,m] - a[l,m]\right)^2 \tag{4}$$

$$\text{with} \quad a'^2 = |a'|^2 = S' = \sum_{i=1}^{N_s} \int_{\theta=0}^{\theta_{\max}} \left|a_i'\right|^2 \sin(\theta)\mathrm{d}\theta. \tag{5}$$

Here a^2 represents the measured streaking spectrogram $S(|\vec{k}|,\tau)$. The calculated complex transition amplitude a_i' is obtained by numerical integration of Eq. (1) in the discrete form. As only an intensity distribution is measured, the phase of the measured spectrogram is zero ($\arg(S) = 0$). The computed streaking spectrogram $S'(|\vec{k}|,\tau)$ is composed from individual spectrograms of the N_s contributing photoelectron bands a_i' with the ionization potential $I_{p,i}$ that are superimposed according to Eq. (3). Following the merit definition from Eq. (4), the complete spectrogram S' does not have a phase ($\arg(S') = 0$), while only the individual complex transition amplitudes have phases associated with them. By expanding the set of equations one obtains:

$$M = \sum_{l=1}^{N_W} \Delta W[l] \sum_{m=1}^{N_\tau} \Delta\tau \left(a'[l,m]^2 + a[l,m]^2 - 2a'[l,m]a[l,m]\right). \tag{6}$$

Similar to Keathley *et al.*, the least-squares minimization is performed in the frequency domain, eliminating the need of a Fourier transform. This minimization routine can be used to estimate the unknown SXR pulse $\tilde{E}_{SXR}(t)$, which is written in the form $\tilde{E}_{SXR}[n] = \alpha[n] \cdot \exp\{i\phi[n]\}$. Performing the least-squares minimization using the merit defined in Eq. (4), and solving the equation for each term $\alpha[n]$ and $\phi[n]$:

$$\frac{\partial M}{\partial \alpha[n]} = 0 \qquad \text{and} \qquad \frac{\partial M}{\partial \phi[n]} = 0. \tag{7}$$

The derivatives of the merit function M with respect to $\alpha[n]$ and $\phi[n]$ lead to the following equations:

$$\begin{aligned} \frac{\partial M}{\partial \alpha[n]} &= \textstyle\sum_{l=1}^{N_W} \Delta W[l] \sum_{m=1}^{N_\tau} \Delta\tau \left(\frac{\partial |a'[l,m]|^2}{\partial \alpha[n]} + \frac{\partial |a[l,m]|^2}{\partial \alpha[n]} - 2\frac{\partial a'[l,m]a[l,m]}{\partial \alpha[n]}\right) \\ &= \textstyle\sum_{i=1}^{N_s} \sum_{j=1}^{N_\theta} \Delta\theta[j] \sum_{l=1}^{N_W} \Delta W[l] \sum_{m=1}^{N_\tau} \Delta\tau \\ &\quad \left(\frac{\partial |a_i'[l,m]|^2 \sin(\theta_j)}{\partial \alpha[n]} - \frac{a[l,m]}{a'[l,m]} \frac{\partial |a_i'[l,m]|^2 \sin(\theta_j)}{\partial \alpha[n]}\right) \end{aligned} \tag{8}$$

$$\begin{aligned} \frac{\partial M}{\partial \phi[n]} &= \textstyle\sum_{i=1}^{N_s} \sum_{j=1}^{N_\theta} \Delta\theta[j] \sum_{l=1}^{N_W} \Delta W[l] \sum_{m=1}^{N_\tau} \Delta\tau \\ &\quad \left(\frac{\partial |a_i'[l,m]|^2 \sin(\theta_j)}{\partial \phi[n]} - \frac{a[l,m]}{a'[l,m]} \frac{\partial |a_i'[l,m]|^2 \sin(\theta_j)}{\partial \phi[n]}\right). \end{aligned} \tag{9}$$

Optics EXPRESS

Here we have used the following relation for the measured spectrogram a:

$$\frac{\partial a}{\partial \alpha} = 0. \tag{10}$$

Combining the results from Eq. (8) and (9) with Eq. (7) leads to the following set of equations:

$$0 = \sum_{i=1}^{N_s} \sum_{j=1}^{N_\theta} \Delta\theta[j] \mathrm{Im}\left(e^{i\phi[c]}(\tilde{\Gamma}_i[c] + \tilde{\beta}_i[c])\right) \sin(\theta_j) \tag{11}$$

$$\begin{aligned} 0 = {} & \alpha[c] \sum_{i=1}^{N_s} \sum_{j=1}^{N_\theta} \Delta\theta[j] \sum_{l=1}^{N_W} \Delta W[l] \sum_{m=1}^{N_\tau} \Delta\tau |\tilde{d}_{(i,|k[l]+A[n+Lm]|,\theta_j)}|^2 \sin(\theta_j) \\ & + \sum_{i=1}^{N_s} \sum_{j=1}^{N_\theta} \Delta\theta[j] \mathrm{Re}\left(e^{i\phi[c]}(\tilde{\Gamma}_i[c] + \tilde{\beta}_i[c])\right) \sin(\theta_j), \end{aligned} \tag{12}$$

where $\tilde{\beta}_i(c)$ and $\tilde{\Gamma}_i(c)$ are defined as:

$$\begin{aligned} \tilde{\Gamma}_i(c) = {} & \sum_{l=1}^{N_W} \Delta W[l] \sum_{m=1}^{N_\tau} \Delta\tau \sum_{n=1,n\neq c}^{N_E} \Delta t^2 \tilde{d}_{(i,|k[l]+A[n+Lm]|,\theta_j)} \\ & \cdot \tilde{d}^*_{(i,|k[l]+A[n+Lm]|,\theta_j)} \tilde{E}^*_{SXR}[n] \cdot e^{\{i(I_{p,i}+k[l]^2/2)\Delta t(c-n)\}} \\ & \cdot e^{\left\{i\Delta t \sum_{b=n+Lm}^{N_A} \Phi(l,b)\right\}} \cdot e^{\left\{-i\Delta t \sum_{b=c+Lm}^{N_A} \Phi(l,b)\right\}} \end{aligned} \tag{13}$$

$$\begin{aligned} \tilde{\beta}_i(c) = {} & i \sum_{l=1}^{N_W} \Delta W[l] \sum_{m=1}^{N_\tau} \Delta\tau \Delta t d_{(i,|k[l]+A[n+Lm]|,\theta_j)} \\ & \cdot e^{\{i(I_{p,i}+k[l]^2)\Delta t c\}} e^{\left\{-i\Delta t \sum_{b=c+Lm}^{N_A} \Phi(l,b)\right\}} \frac{a_i'^*[l,m] a[l,m]}{a'[l,m]}. \end{aligned} \tag{14}$$

By adding Eqs. (11) and (12), one finds for $\tilde{E}_{SXR}[c] = \alpha[c]e^{i\phi[c]}$ the following equation:

$$\tilde{E}_{SXR}[c] = \frac{-\sum_{i=1}^{N_s} \sum_{j=1}^{N_\theta} \Delta\theta[j] \left(\tilde{\Gamma}_i[c] + \tilde{\beta}_i[c]\right)^* \sin(\theta_j)}{\sum_{i=1}^{N_s} \sum_{j=1}^{N_\theta} \Delta\theta[j] \sum_{l=1}^{N_W} \Delta W[l] \sum_{m=1}^{N_\tau} \Delta\tau |d_{i,|k[l]+A[c+Lm]|,\theta_j}|^2 \sin(\theta_j)}. \tag{15}$$

The optimization of the parameters describing the IR field is independent of the SXR and the number of initial states involved. The Brent minimization [34, 35] procedure is performed as described by Keathley *et al.* [26]. A flow-chart of the ML-VTGPA method including the photoelectron angular distribution is depicted in Fig. 4(A). By minimizing the error between the measured and retrieved spectrograms, new guesses for $\tilde{E}_{SXR}(t)$ and $A(t)$ are obtained and used for the next iteration of the algorithm. The minimization procedure is performed until the convergence criterion (mean square error (MSE), square root of the intensity difference between the normalized streaking spectrograms S and S') is reached.

4. Results and discussion

In this section, the reconstruction using the multi-line VTGPA (ML-VTGPA) and its application to streaking spectra with large polar angle integration is demonstrated to show an accurate and complete reconstruction of the pulse parameters for the attosecond as well as the streaking IR pulses. For this purpose, several streaking spectrograms are computed using Eq. (3). The photoionization matrix elements for the target gas were obtained from Kheifets [36] for the case of xenon (shown in Fig. 4(B)) and from Bhardwaj [37] in the case of helium. For the xenon ionization potentials the following values were used: $I_{p,5p} = 12.1$ eV, $I_{p,5s} = 23.4$ eV [32], and $I_{p,4d} = 67.5$ eV [33]. In this section, the simulated streaking spectrograms from the numerical experiments are referred to as input spectrum $S(E, \tau)$ and are used as the input to the retrieval algorithms. The corresponding simulation parameters are therefore called input vector potential $A_{inp}(t)$ and input SXR pulse with the intensity $I_{inp}(t)$ and phase $\Phi_{inp}(t)$. For some cases in subsection 4.1 the ML-VTGPA retrieval result is compared to the LSGPA method (or FROG-CRAB).

Optics EXPRESS

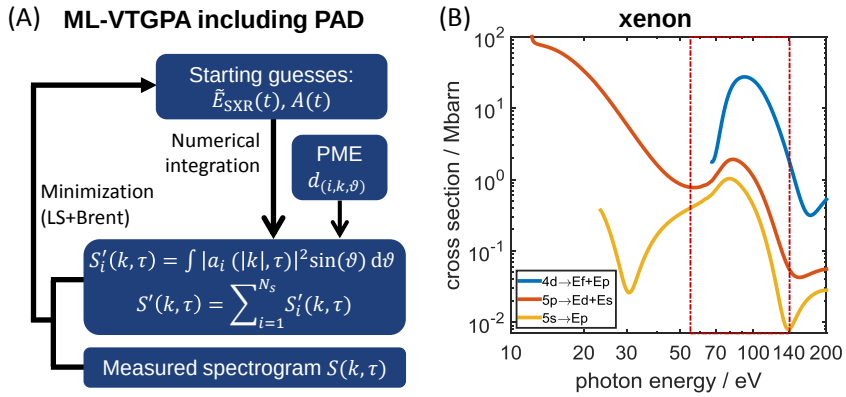

Fig. 4. Flow-chart of the multi-line VTGPA including photoelectron angular distributions and photoionization cross sections of xenon. (A) Flow-chart of the multi-line VTGPA including photoelectron angular distribution (PAD). Starting guesses for $\tilde{E}_{SXR}(t)$ and $A(t)$ are used together with the PMEs $d_{(i,k,\theta)}$ for the numerical integration of the streaking Eq. (1) to obtain $S'(|\vec{k}|,\tau)$ from the N_s contributing streaking spectra S_i' from the individual shells integrated over the acceptance polar angle θ of the photoelectron spectrometer. This is compared with the measured (input) spectrogram $S(|\vec{k}|,\tau)$ to minimize the error using the merit function in Eq. (6) with the least-squares (LS) method and Brent's minimization. (B) Cross sections for the 5s, 5p, and 4d shells calculated from the complex photoionization matrix elements (PMEs) [36]. The red box indicates the photon energy range, where the numerical experiments presented in section 4.1 are performed, which also corresponds to the energy range typically covered by Ti:Sa driven attosecond sources. The strong energy dependence of the cross sections has to be accounted for in pulse-retrieval methods for broadband pulses.

4.1. *Multi-line VTGPA*

Figure 5(A) shows the input streaking trace $S(E,\tau)$ for the case of a Gaussian SXR pulse with a pulse duration of $\tau_{SXR} = 350$ as (FWHM) streaked by a few-cycle NIR pulse. The pulse duration $\tau_{SXR} = 350$ as for an unchirped pulse corresponds to a bandwidth of $\Delta E = 5.2$ eV at a central energy of $W_0 = 110$ eV (cf. Fig. 6(A)). Since the SXR pulse ionizes from the 4d, 5p, and 5s shells of xenon, all three corresponding PMEs are incorporated in the calculations and N_s is set to three. The target gas was modeled using the calculated PMEs from Kheifets [36]. The NIR pulse duration of $\tau_{IR} = 3.5$ fs (FWHM) corresponds to a typical pulse obtained from a hollow-core fiber after spectral broadening and compression of the output of a Titanium:Sapphire amplifier ($\lambda_c = 800$ nm), which is state-of-the-art in a number of laboratories. The center wavelength is blue-shifted to the visible spectral region at $\lambda_c = 650$ nm with a peak intensity of $I_0 = 2.1 \cdot 10^{12}$ Wcm^{-2}. A second-order temporal phase of $-1.97 \cdot 10^{-6}$fs^{-2} (linear chirp) and an uncompensated third-order temporal phase of $1.17 \cdot 10^{-8}$fs^{-3} (quadratic chirp) were assumed, for the streaking trace $S(E,\tau)$ presented in Fig. 5(A).

For the reconstruction procedure, the vector potential of the IR streaking pulse is defined as $A(t) = A_0^{(N)}(t)\cos\alpha(t)$, where the field envelope $A^{(N)}$ is described by a cubic spline interpolation with N supporting points. The phase $\alpha(t)$ is expanded in a power series $\alpha(t) = \alpha_0 + \alpha_1 t + \alpha_2 t^2 + \alpha_3 t^3 + \ldots + \alpha_k t^k$, where α_0 corresponds to the CEP, α_1 to the central angular frequency and higher order chirp terms α_2 to α_k. For the example presented here, $N = 7$ supporting points and $k = 4$ orders were chosen for the envelope function and the power expansion of the carrier frequency, respectively. Thus, the femtosecond streaking IR pulse is fully represented by just $N + k = 11$ quantities that have to be minimized by Brent's algorithm [34, 35]. Due

Optics EXPRESS

to the analytical description of the vector potential/electric field of the streaking pulse no additional noise is introduced during the retrieval process. For the reconstruction, an initial guess for these 11 quantities is needed, which is obtained by performing a center-of-energy (COE) analysis of the streaking spectrogram. For the initial guess of the SXR pulse, a Gaussian envelope $\tilde{E}_{\mathrm{SXR}}(t) = E_0 \exp\{-(t-t_0)^2/\left(\tau_{\mathrm{SXR}}/\sqrt{2\ln(2)}\right)^2\}$ is assumed, where E_0 is the peak field amplitude, t_0 a shift in time, and τ_{SXR} the SXR pulse duration.

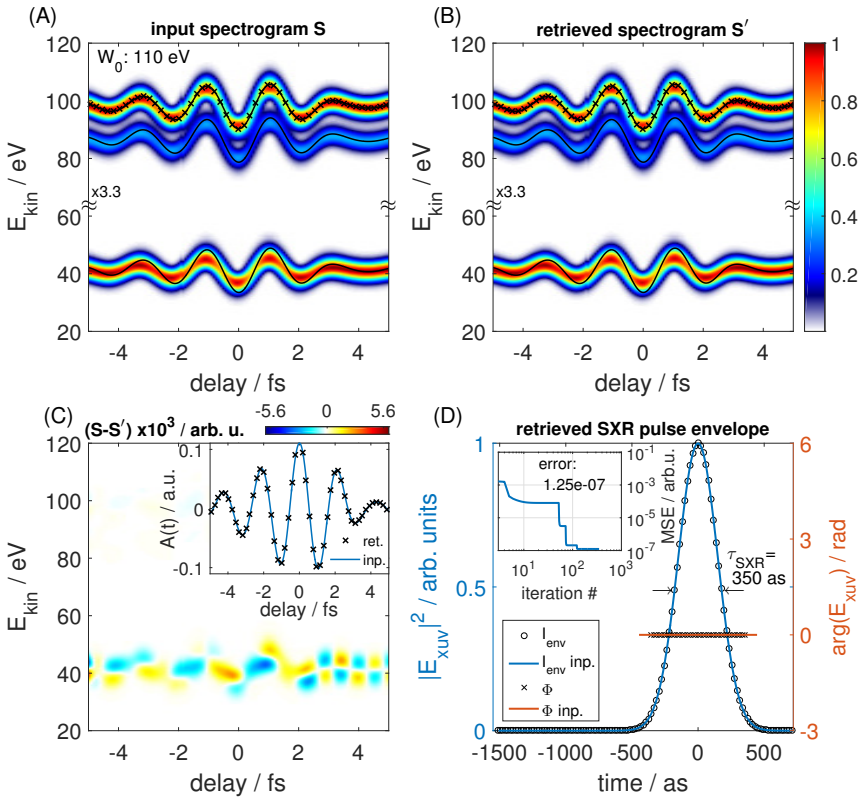

Fig. 5. Multi-line streaking spectrogram in xenon. Simulated (A) and reconstructed (B) streaking spectrogram to test the ML-VTGPA algorithm with an attosecond pulse duration of $\tau_{\mathrm{SXR}} = 350$ as in xenon including the PMEs for the 5p, 5s (both multiplied by 3.3, for better visibility of all photoelectron bands) and 4d photoelectron bands. The input vector potential $A(t)$ (blue line) and the reconstructed vector potential (black crosses) are scaled and plotted on top of the 5p photoelectron line for comparison. (C) False color representation of the difference between S and S' multiplied by three orders of magnitude. The residual mean square error between measured and reconstructed spectrogram was found to be $1.25 \cdot 10^{-7}$ after 350 iterations of the algorithm. The unscaled vector potentials (input and retrieved) are also shown as an inset to the panel. (D) Reconstructed SXR pulse parameters amplitude $I_{\mathrm{env}}(t)$ and phase $\Phi(t)$ (black circles and crosses) for detailed comparison with the input SXR pulse parameters (blue, red lines).

Figure 5(B) shows the retrieved streaking spectrogram $S'(E,\tau)$ for all electron shells, together with the retrieved and scaled vector potential $A(t)$ as black crosses on top of the 5p streaking line. The thin blue line represents the input vector potential used to calculate the streaking spectrogram. Input and reconstructed spectrogram have been scaled the same way to resemble the streaking trace of the 5p photoelectrons. The same scaling was used for the 4d electrons. By comparing the

Optics EXPRESS

4d photoelectron line with $A(t)$ the reduced streaking amplitude is clearly visible, due to the lower initial momentum $\vec{k}_0$ of the 4d electrons. The 5s, 5p lines have been scaled by a factor of ≈ 3.3 in intensity, due to the lower cross section (cf. Fig. 4(B)), for better visibility in the false color plot.

For better comparison between simulated $S(E,\tau)$ and reconstructed $S'(E,\tau)$ spectrogram the difference between panel (A) and (B) is shown in panel (C), where the normalized intensity difference at all energy and delay points is always better than 10^{-2}. In the difference plot no streaking structure is visible after the convergence of the algorithm. The overall residual mean square error between measured and reconstructed spectrogram was found to be $1.25 \cdot 10^{-7}$ after 350 iterations of the algorithm. In Figure 5(D), the intensity envelope $I_{\mathrm{env}}(t)$ and the phase $\Phi(t)$ of the SXR pulse are shown. The perfect agreement between all input and retrieved quantities clearly demonstrates that the ML-VTGPA algorithm retrieves, both the SXR and the IR pulse, completely with very high fidelity within the PME corrected SFA.

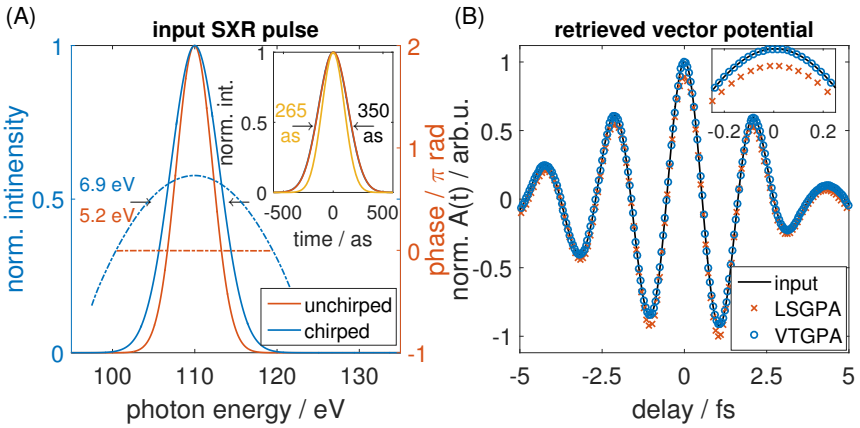

Fig. 6. SXR input pulse and retrieved vector potential. (A) Chirped (blue) and unchirped (orange) SXR input pulse in spectral and temporal (inset) domain. The $\tau_{\mathrm{SXR}} = 350\,\mathrm{as}$ used in Fig. 5 centered around $W_0 = 110\,\mathrm{eV}$ with a bandwidth of a $\Delta E = 5.2\,\mathrm{eV}$. For the corresponding chirped SXR pulse from Fig. 7, the bandwidth increases to $\Delta E = 6.9\,\mathrm{eV}$, and the spectral phase has a quadratic energy dependence (blue dash-dotted line), compared to the flat spectral phase for the previous case (orange dash-dotted). The inset also shows the FTL pulse duration for the increased bandwidth case (yellow), that corresponds to a $\tau_{\mathrm{SXR,FTL}} = 265\,\mathrm{as}$ pulse. (B) LSGPA (orange crosses) and ML-VTGPA (blue circles) retrieved vector potential for the case presented in Fig. 7, in comparison with the input vector potential (black line).

For the numerical experiment presented in Fig. 7, the same input parameters as described for the previous experiment have been used, except that the SXR pulse was strongly chirped with a (temporal) chirp of $-1.00 \cdot 10^{-5}\mathrm{as}^{-2}$, which is shown in Fig. 6(A) in comparison to the unchirped case, leading to an increased bandwidth of $\Delta E = 6.9\,\mathrm{eV}$ and corresponding to a Fourier transform limited pulse duration of $\tau_{\mathrm{SXR}} = 265\,\mathrm{as}$. The chirp is also visible in Fig. 7(A), where a strong asymmetry in the intensity distribution of the streaking trace between regions of positive and negative vector potential can be observed together with an increased streaking amplitude by comparing Fig. 5(A) with 7(A). The apparent increase in the streaking amplitude leads to erroneous reconstruction results for LSGPA due to the CMA (cf. [31]). For these narrowband pulses discussed so far the individual photoemission lines are clearly separated, even the 5p and 5s lines start to merge for the chirped attosecond pulse.

For this case, the ML-VTGPA results are compared with LSGPA [25, 38] results using the software ATTOGRAMM [38]. The obtained streaking traces are shown in Fig. 7(C) and 7(E)

Optics EXPRESS

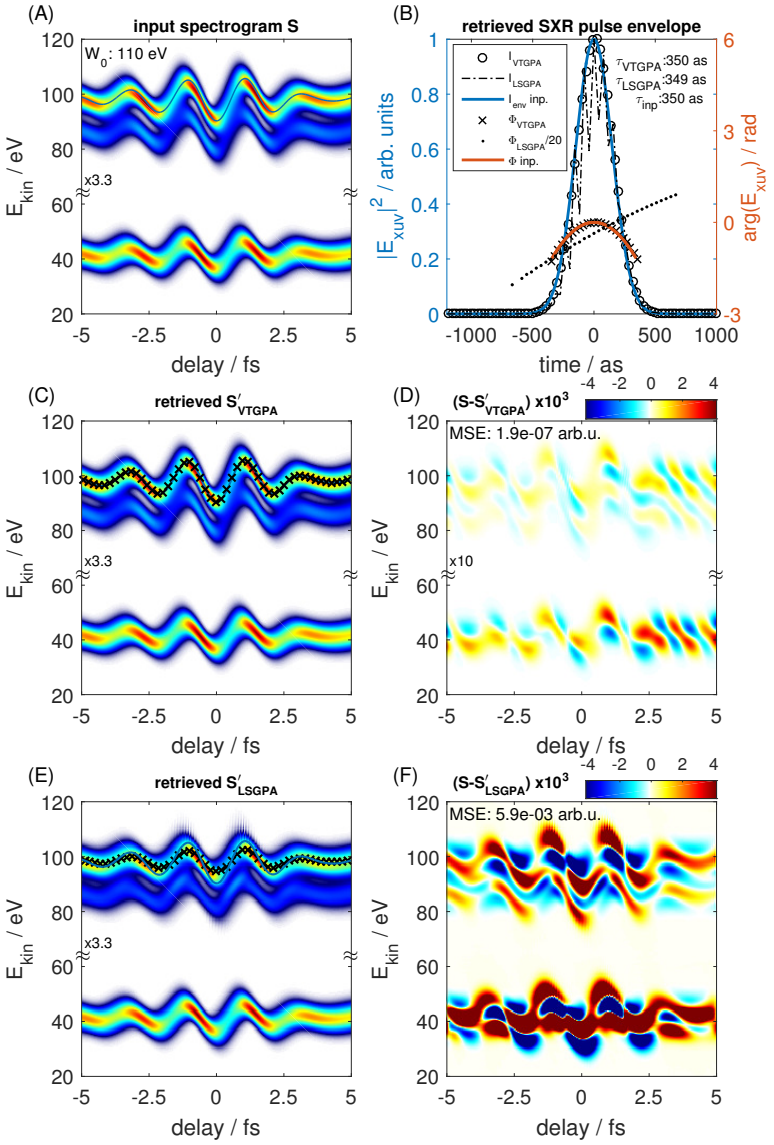

Fig. 7. Reconstruction of a multi-line streaking spectrogram in xenon for a chirped 350 as SXR pulse, using the ML-VTGPA and LSGPA methods. (A) Simulated input streaking spectrogram for xenon including the PMEs for the 5p, 5s (both multiplied by 3.3, for better visibility) and 4d photoelectron bands. The input parameters are the same as for Fig. 5, except for a second order SXR chirp of $-1.00 \cdot 10^{-5}\mathrm{as}^{-2}$, leading to larger bandwidth and broader lines that partially overlap. For reconstruction the ML-VTGPA (C, D) and the LSGPA (E, F) methods have been used. The retrieved attosecond SXR pulses are shown in panel (B) together with the obtained pulse duration, while the obtained vector potentials are shown on top of the retrieved spectrogram S' for both methods. The input pulses are given by blue lines, while the reconstructed vector potentials are given by the black crosses (Every 40th data point is plotted for better visibility.). It has to be noted that the panels (D) and (F) are using the same color scale, for a better comparison between the two methods. In panel (D) the upper part of the plot ($E_{\mathrm{kin}} > 65\,\mathrm{eV}$) has been amplified by x10 for a better visibility of the residuals. Panel (A), (C), and (E) use the same color scale as used before for input and reconstructed spectrogram, c.f. Fig. 5.

Optics EXPRESS

together with the false-color representation of the deviation between simulated S and reconstructed S' streaking spectrogram, for the case of ML-VTGPA 7(D) and LSGPA 7(F). It has to be noted that the panels (D) and (F) are using the same color scale, for a better comparison between the two methods. Already from this representation, a much better fidelity of the VTGPA is visible as only unstructured patterns remain in the difference plot, while in the case of LSGPA an oscillating streaking trace is still visible with larger deviations from the input (darker color). For LSGPA, the error is dominated at high streaking amplitudes, which can be explained by the CMA for the ponderomotive shift of the photoelectrons. For the ML-VTGPA reconstruction the MSE after 500 iterations of the algorithm is already below $2 \cdot 10^{-7}$, while the LSGPA reconstruction does not go below $5.9 \cdot 10^{-3}$ for a calculated spectrogram without noise.

The same behavior can be observed by comparing the reconstructed vector potential $A(t)$ (black crosses, every 40th data point for better visibility) that are overlaid on the panels 7(C) and 7(E) together with input vector potential (blue line). Here also, an excellent agreement between retrieved and input pulse parameters can be found for ML-VTGPA method. As expected the LSGPA method retrieves a vector potential similar to the input pulse, but with an underestimated amplitude. A direct comparison between LSGPA (orange crosses) and ML-VTGPA (blue circles) normalized vector potential is presented in Fig. 6(B) together with the input pulse (black line). Both methods retrieve for such narrowband pulses a similar vector potential. The ML-VTGPA shows higher fidelity in the reconstruction, as the strongest amplitude is correctly reconstructed, while the peak amplitude of the LSGPA retrieved vector potential is only 85% of the input vector potential. The lower streaking amplitude of the retrieved IR pulse, therefore leads to the strong pattern in the difference plot between input and retrieved streaking trace, where the streaking trace is still visible, as shown in panel (F) of the figure. In panel (B), the intensity distributions and phase (VTGPA: black circles and crosses, LSGPA: dash dotted line and dots) of the reconstructed SXR pulses are presented together with the original pulse (blue and red line). Both algorithms reconstruct the (correct) pulse duration. For the LSGPA reconstruction an amplitude oscillation remains on the pulse that is also visible in the retrieved streaking spectrogram in panel (E). This can be attributed to the different cross sections of the photoelectron band. As soon as the 4d line is reconstructed individually the intensity fluctuation disappears, but the high MSE remains. Calculating the input streaking spectrograms within the CMA the MSE decreases to $\ll 10^{-5}$. However, the amplitude of the vector potential is still incorrectly reconstructed.

Very recently, we have demonstrated attosecond streaking with ultrabroadband SXR pulses spanning the spectral region from 60 eV to 180 eV (beamline limited), supporting attosecond pulses down to 34 as [16]. For those streaking experiments, xenon has been used, due to the higher cross sections compared to helium in the energy range around 100 eV. For photon energies between 50 and 140 eV, xenon is a suitable choice since the cross sections do not drop by more than two orders of magnitude. Since the cross section of helium or any other noble gas changes by several orders of magnitude over such a broad range of energies, this influence cannot be neglected for a reliable pulse reconstruction, as the spectral amplitude and phase and therefore the temporal shape of the photoelectron wave packet can be strongly modified as compared to the attosecond pulse to be measured.

To show the capabilities of the new ML-VTGPA method a streaking spectrogram for a chirped $\tau_{\mathrm{SXR}} = 55$ as SXR pulse supporting a pulse duration of $\tau_{\mathrm{SXR}} = 50$ as (second order SXR chirp of $4 \cdot 10^{-4}$ as^{-2}) centered at a photon energy of $W_0 = 110$ eV has been calculated with the focus on the overlapping photoelectron band 5s, 5p, setting N_{s} to two. There the streaking effect is more pronounced compared to the 4d photoelectron band, due to the initially higher kinetic energy. All other pulse parameters were chosen to be the same like in the first example, presented in Fig. 5. Here, only the ML-VTGPA retrieved streaking spectrogram $S'_{\mathrm{VTGPA}}(E, \tau)$ is presented together with the difference between $S - S'_{\mathrm{VTGPA}}$ in Fig. 8 (A) and (B). It has to be noted that the difference plot was multiplied by 10^3. A maximum deviation $\ll 7 \cdot 10^{-3}$ was found, while the overall mean

Optics EXPRESS

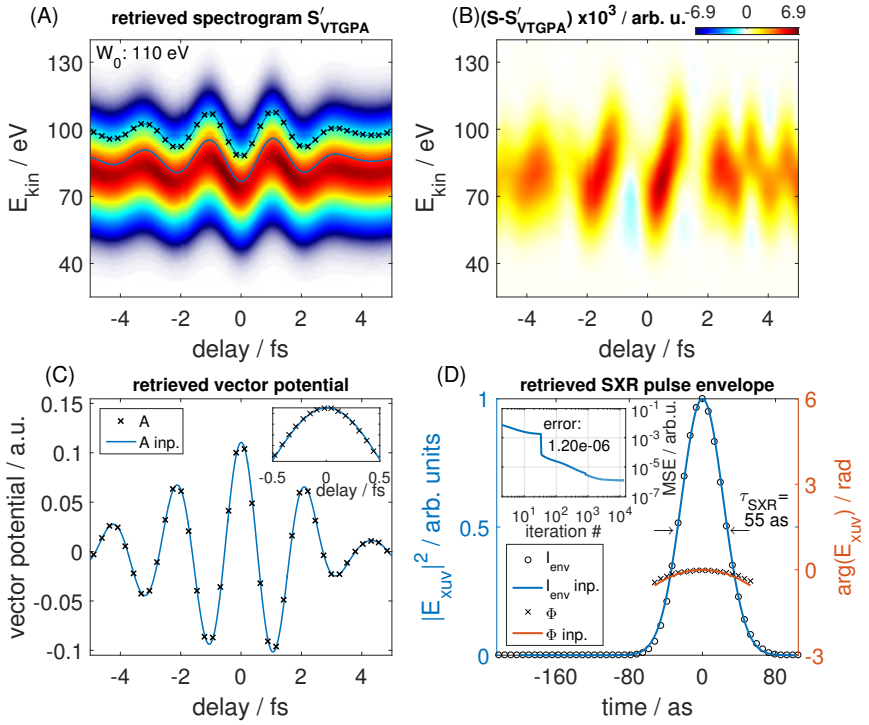

Fig. 8. Multi-line streaking spectrogram in xenon for a chirped 55 as SXR pulse with overlapping 5s, 5p photoelectron band. Retrieved (A) streaking spectrogram for a chirped $\tau_{\mathrm{SXR}} = 55$ as SXR pulse with a spectrum supporting $\tau_{\mathrm{SXR}} = 50$ as at a center energy of $W_0 = 110$ eV in the region of overlapping xenon 5p, 5s photoelectron band including the PMEs. The input parameters are the same as for Fig. 5. The blue solid lines represent the vector potential of the IR pulse $A(t)$ used for the simulation at the central kinetic energies $(W_0 - I_{\mathrm{p},i})$ of the xenon lines, while the reconstructed vector potential of the streaking pulse is given by the black crosses. The difference between calculated and reconstructed spectrogram is given in panel (B), where the maximum deviation is $\ll 2.5 \cdot 10^{-3}$, while the overall MSE of the reconstruction is already below $1.5 \cdot 10^{-6}$ after 12000 iterations (inset to panel (D)). In panel (C) every 40th point of the retrieved vector potential $A(t)$ is plotted together with the input pulse (blue) while in the inset every 10th retrieved point is shown. Panel (D) shows the retrieved SXR pulse parameter $I_{\mathrm{env}}(t)$ and $\Phi(t)$ together with the input pulse. Panel (A) uses the same color scale as used before for input and reconstructed spectrogram, c.f. Fig. 5.

Optics EXPRESS

squared error of the reconstruction is already below $< 1.5 \cdot 10^{-6}$ after 12000 iterations. Every 40th point in time of the scaled retrieved vector potential (black crosses) is shown together with the simulation input (blue lines) in panel (A) and (B). The blue lines of the vector potentials are given at the initial kinetic energies of the 5s ($W_0 - 23.4$ eV) and 5p photoelectron band ($W_0 - 12.1$ eV). The energy shift of the photoelectron band with respect to center-of-energy of the spectrogram is due to the strongly varying PMEs (cf. Fig. 4(B)). In the panels (C) and (D) the retrieved quantities $A(t)$, $I_{\mathrm{env}}(t)$, and $\Phi(t)$ are presented together with the input pulses. In the inset to panel (C) the the vector potential (every 10th point) is presented at its highest amplitude to demonstrate the high quality of the reconstruction, due to the full implementation of the SFA without CMA. During the application of the ML-VTGPA method it was found that the vector potential converges typically faster compared to the SXR pulse envelope (cf. [26]). Therefore, the algorithm allows to run patterns for the optimization of $\tilde{E}_{\mathrm{SXR}}(t)$ and $A(t)$, where typically 100 iterations for $\tilde{E}_{\mathrm{SXR}}(t)$ are executed before 10 iterations for the optimization of $A(t)$ are performed, to obtain faster convergence for the streaking spectrogram. To summarize, also in this case, an excellent agreement for SXR and IR streaking pulse was found.

Using mid-IR laser sources or OPAs for wavelength conversion, multiple groups have recently demonstrated ultra-broadband SXR continua with photon energies covering the water window region [11–15]. Here, it is shown, that the ML-VTGPA method, when reduced to a single line ($N_{\mathrm{s}} = 1$, similar to the original implementation [26]), is also suitable for attosecond pulses shorter than the atomic unit in time. To show this, a streaking trace with a $\tau_{\mathrm{SXR}} = 20$ as, chirp-free (flat phase) pulse at a central photon energy of $W_0 = 260$ eV was reconstructed using the ML-VTGPA method, where the PMEs for helium [37, 39] were used. The retrieved streaking spectrogram is shown in Fig. 9(A). Even though the helium cross section is comparably flat with respect to the other rare gases typically used (Ne, Kr, Xe), the COE of the streaking trace is not around the initial kinetic energy of the photoelectrons. On top of the streaking spectrogram, the retrieved vector potential $A(t)$ is plotted as black crosses together with the input field at the initial kinetic energy of the helium photoelectrons ($W_0 - 24$ eV=236 eV) in panel (A). The black crosses follow perfectly the input vector potential (blue line). The difference between original and retrieved spectrogram is shown in panel (B). No remaining streaking structure can be found in the difference plot, demonstrating again the high fidelity of the ML-VTGPA reconstruction method, also for these ultrashort attosecond pulses. In Fig. 9(C), the retrieved SXR pulse is shown together with the input pulse. As inset to the panel, the evolution of the MSE during the reconstruction is shown.

In this section we have first demonstrated the application of the ML-VTGPA method to narrow- and broadband SXR spectra, corresponding to long ($\tau_{\mathrm{SXR}} = 350$ as) and short chirped ($\tau_{\mathrm{SXR}} = 55$ as) pulses for the case of the overlapping photoelectron originating from the 5s and 5p shells in xenon. We have demonstrated the reconstruction of chirped SXR pulses and IR streaking pulses with high fidelity. For the case of a chirped attosecond SXR pulse ($\tau_{\mathrm{SXR}} = 350$ as) and a chirped IR pulse we have compared our results with the commonly used LSGPA method. While we obtained an excellent reconstruction for the ML-VTGPA method (MSE$< 2 \cdot 10^{-7}$), in terms of IR vector potential and SXR pulse envelope and phase, we found that the LSGPA (MSE$< 6 \cdot 10^{-3}$) reconstructed pulse envelope shows artifacts, the phase shows a larger discrepancy to the input pulse and the vector potential amplitude is underestimated. The former is attributed to the different cross sections of the photoelectron band while the latter is explained by the central-momentum approximation. Second, we have further shown the retrieval of a chirped $\tau_{\mathrm{SXR}} = 55$ as SXR pulse centered at photon energies around $W_0 = 110$ eV, where xenon as the target gas shows the highest cross section for the 5p photoelectron line. Due to the small difference in ionization ($I_{\mathrm{p,5s}} - I_{\mathrm{p,5p}} = 11.3$ eV) and the large bandwidth of the SXR pulse ($\Delta W = 30$ eV), the photoelectron bands fully overlap. Therefore only the ML-VTGPA method is suitable to retrieve SXR and IR streaking pulse with highest fidelity, without overestimating the bandwidth of the SXR pulse. Third we have shown the excellent retrieval of an isolated SXR pulse shorter than the atomic

Optics EXPRESS

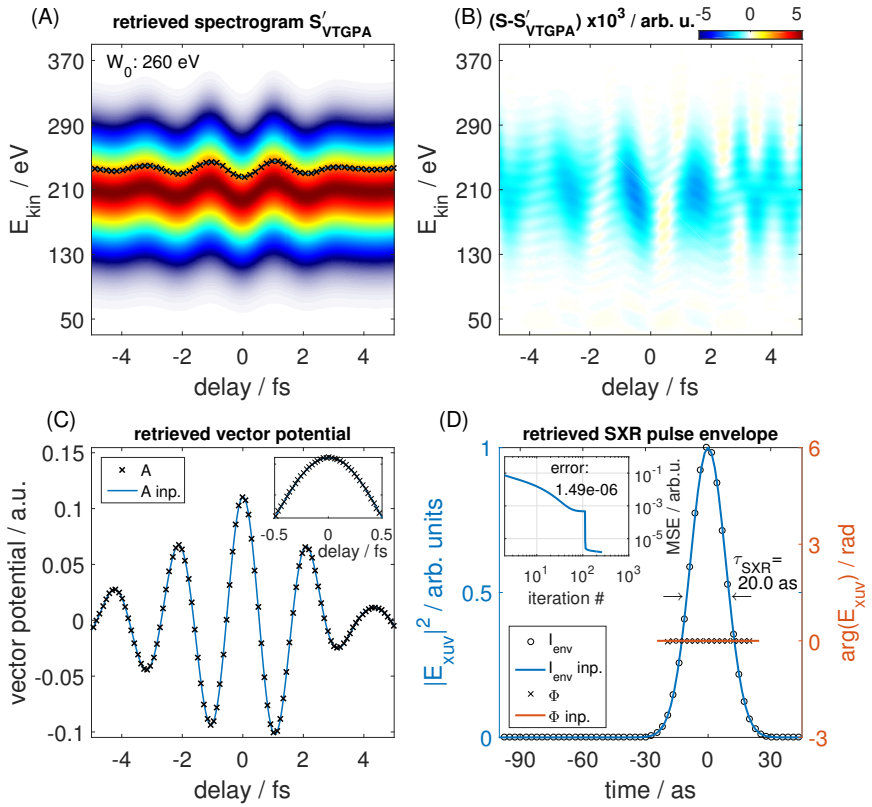

Fig. 9. Streaking spectrogram in helium for a 20 as SXR pulse centered at 260 eV. Reconstructed (A) streaking spectrogram for an SXR pulse duration $\tau_{\mathrm{SXR}} = 20$ as with a central photon energy of $W_0 = 260$ eV in He including the PMEs calculated by Bhardwaj *et al.* [37]. The input parameters for the vector potential of the IR streaking pulse $A(t)$ are the same as in example 1. The difference between calculated and reconstructed spectrogram is given in panel (B), where the maximum deviation is $\ll 2 \cdot 10^{-2}$, while the overall error (MSE) of the reconstruction is after approx. 300 iterations already below $\ll 2 \cdot 10^{-6}$ (inset to panel (D)). The scaled reconstructed (black crosses) and the input (blue line) vector potential are given together at the initial kinetic energy of the photoelectrons ($W_0 - I_{\mathrm{p}}$) in panel (A). Panel (C) shows A(t) on the atomic unit scale. Every 40th point of the retrieved A(t) is shown, while in the inset every 10th point around the maximum of A(t) is shown. In panel (D), the retrieved SXR pulse envelope and phase are shown together with the input pulse. As inset to the panel, the evolution of the MSE during the reconstruction is plotted. Panel (A) uses the same color scale as used before for input and reconstructed spectrogram, c.f. Fig. 5.

Optics EXPRESS

unit in time centered at $W_0 = 110$ eV, mimicking the broadband SXR continua generated using mid-IR laser sources. For this purpose we have chosen helium as target medium, as it offers the flattest cross section over the energy bandwidth of the SXR pulse.

4.2. ML-VTGPA including photoelectron angular distributions

Here, we study the reconstruction of attosecond pulses from partially angle-integrated streaking spectrograms of helium, testing the reconstruction for the integration over different ranges of the polar angle and demonstrating the influence of angle integration on the retrieval. We test the method to investigate the influence of the collection angle θ on the streaking spectrogram and its reconstruction by performing a numerical experiment where a streaking spectrogram in helium was calculated within the SFA using Eq. (3), where we integrated over a photoemission polar angle of $0° \leq \theta \leq 120°$ in steps of 1°. It has to be noted that Eq. (1) incorporates the full angle-dependent PMEs. However, in this section, we have approximated for demonstration purposes, the angle-resolved PMEs by the PMEs parallel to the polarization of the light. The obtained spectrogram is presented in Fig. 10(A).

For the reconstruction, the maximal acceptance angle $\theta_{\max}$ was varied between 90° and 140°, while the integration was always performed over five equidistant steps ($N_\theta = 5$). The reconstructed vector potential $A(t)$ and SXR pulse envelopes $I_{\text{env}}(t)$ are presented in Fig. 11 (panels (A) and (B), respectively), as a function of the maximum acceptance angle $\theta_{\max}$ together with the MSE in panel Fig. 11(C). It can be seen, that for different angles of integration, the convergence varies drastically by as much as two orders of magnitude between the best ($\theta_{\max} = 120°$) and the worst ($\theta_{\max} = 90°$) reconstruction already after 45 iterations of the algorithm, as shown in Fig. 11(C). For the reconstructions with acceptance angles between $100° \leq \theta_{\max} \leq 140°$, the smallest residual error is obtained for $\theta_{\max} = 120°$, which indeed corresponds to the assumption made for the input spectrogram. In panels (A) and (B) the simulation input is given as black crosses for comparison.

However, a tolerance of $-5°$ and $+10°$ in the maximum acceptance angle $\theta_{\max}$ of the detector allows for the reconstruction of the main features of the attosecond SXR and femtosecond IR pulses with an accuracy better than 95 %, as shown in Fig. 11(A) and (B) for the retrieved vector potential and the SXR envelope, respectively. The influence of the angle integration is more significant on the IR pulse, where especially an underestimation of the collection angle leads to a severe underestimation of the IR-pulse intensity and pulse duration (Fig. 11(A)). However, the algorithm with its constraints on the vector potential $A(t)$, can still reconstruct with an error of < 10 % if the acceptance angle of the spectrometer is known within a range of ±10°, where LSGPA fails completely. In principle, a single streaking trace with a narrowband SXR pulse (long pulse duration) is sufficient for an experimental calibration of the spectrometer-specific acceptance angle of the MB-TOF.

This shows that our algorithm can reconstruct the streaking spectrograms with very high fidelity even though a large acceptance angle of the electron spectrometer leads to a more complicated streaking spectrogram than before.

Figure 10(B) shows the reconstructed streaking spectrogram with the lowest mean squared error of all reconstructions, with a collection angle of $\theta_{\max} \leq 120°$ using the ML-VTGPA including PAD. In panel (C), a false color representation of the difference between simulated and reconstructed streaking trace multiplied by 100 is presented for a better visual comparison. There is clearly no remaining streaking spectrogram visible after the convergence of the algorithm that proves the high fidelity of our reconstruction. In panel (D), the SXR pulse used for the simulation (intensity envelope and phase: red and blue lines) is shown together with the corresponding reconstructed quantities. Not only the pulse duration but also the shape of the pulse matches very well at every point in time. The mean squared error for the reconstruction is presented as an inset to (D), showing the convergence of the algorithm until it is stopped with a residual MSE of

Optics EXPRESS

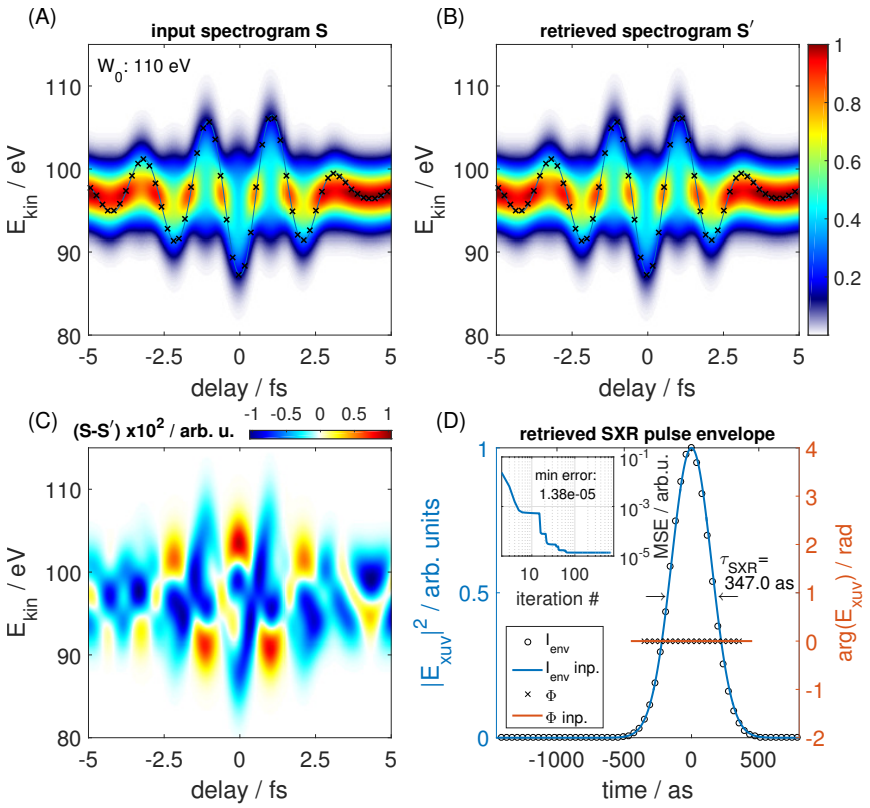

Fig. 10. Angle integrated streaking spectrogram in helium. Simulated input spectrogram S (A) and reconstructed (B) streaking spectrogram S' to test the ML-VTGPA including photoelectron angular distribution with an attosecond pulse duration of $\tau_{\mathrm{SXR}} = 350\,\mathrm{as}$ in helium using the PMEs. For the reconstruction an acceptance angle of $\theta_{\max} = 120°$ has been assumed. Therefore the number of reconstruction angles N_θ was set to 5 with an equidistant distribution between $0 \le \theta \le 120°$. The vector potential $A(t)$ used for the simulation (blue line) reconstructed vector potential (black crosses, every tenth data point) are plotted on top for comparison. (C) False color representation of the difference between simulated and reconstructed streaking trace multiplied by 100, for a better comparison. (D) Simulated SXR pulse (intensity envelope and phase: red and blue lines) together with the corresponding reconstructed quantities. The mean squared error for the reconstruction is presented as an inset to (D), showing a residual MSE $\ll 2 \cdot 10^{-5}$.

Optics EXPRESS

about $2 \cdot 10^{-5}$. This clearly shows that for a large range of collection angles the contribution from different angles have to be taken into account.

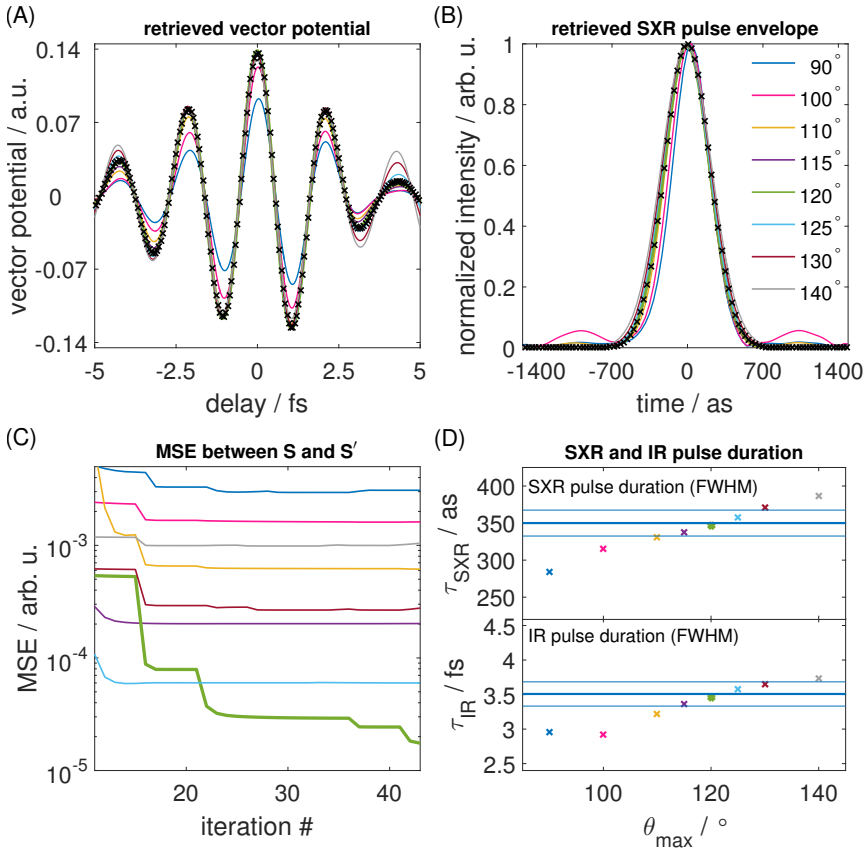

Fig. 11. Reconstructed vector potential and SXR intensity envelope for different acceptance angles of the MB-TOF. Retrieval results for the streaking vector potential $A(t)$ (A) and the attosecond SXR pulse $I_{\mathrm{env}}(t)$ (B) as a function of the acceptance angle of the spectrometer. The input pulses are given by black crosses for comparison. The angle integration was performed over 5 angles ($N_\theta = 5$) with a variation of maximum acceptance angle θ_{max} between 90° and 140°. (C) shows the residual MSE after 45 iterations of the algorithm, where the case of $\theta_{max} = 90°$ already starts to diverge. (D) SXR- and IR-pulse as a function of maximum acceptance angle after convergence of the reconstruction. The input pulse durations (thick blue lines) are shown together with a ±5 % deviation (thin blue lines).

5. Conclusion and outlook

In section 3 of this article we have introduced in detail the full mathematical formalism for the extension of the new attosecond reconstruction method "Volkov-transform generalized projection algorithm" to allow the reconstruction of multiple overlapping photoelectron band including angle integration. The method allows to reconstruct attosecond pulses within the strong-field approximation without Fourier transformation and therefore enables the incorporation of the target-specific complex energy dependent photoionization matrix elements. As the method does not rely on the bandwidth-limiting central-momentum approximation, it is ideally suited for the characterization of ultrashort SXR pulses, where no other attosecond pulse retrieval method

Optics EXPRESS

has till now shown the retrieval of such short pulses including more than one photoemission band with such high rigor. The formalism includes the photoelectron angular distribution into the reconstruction and therefore accounts for the angle-dependence of the streaking process. This allows us to analyze partially angle-integrated (eg. MB-TOF spectra) streaking-spectrograms or by partially integrating angle-resolved spectra (recorded by e.g. velocity map imaging (VMI) spectrometer).

In section 4.1, we have demonstrated numerically that our multi-line algorithm is perfectly suitable for the retrieval of ultrashort SXR pulses and streaking fields from the near- and mid-infrared spectral region. We have shown the reconstruction of short (chirped) ($\tau_{\mathrm{SXR}} \leq 55$ as) and long ($\tau_{\mathrm{SXR}} = 350$ as) SXR attosecond pulses using NIR streaking fields in xenon, leading to partially and fully overlapping streaking spectrograms. The effect of chirped SXR and IR pulses on the streaking spectrogram and the retrieval process have been presented and discussed in detail. Our algorithm demonstrates a high fidelity in the retrieval as seen by comparing the streaking spectrogram as well as input and retrieved pulse. Besides the inclusion of the PMEs, the analytical description of the IR streaking fields ensures a noise-free reconstruction of the vector potential and the corresponding IR field. With laser based X-ray sources reaching photon energies up to 500 eV with reasonable flux, we demonstrate the application of our reconstruction method to reconstruct pulses less than one atomic unit of time (24 as) and covering X-ray absorption edges of most light elements. We have, therefore, presented the accurate and complete characterization of a simulated attosecond pulse of $\tau_{\mathrm{SXR}} = 20$ as, in helium. In the very recent paper by Gaumnitz *et al.* [16], we demonstrated the experimental application of this method, where we retrieved an isolated attosecond pulse generated using a mid-infrared driving laser pulse. Employing the ML-VTGPA method, we have obtained a pulse duration of $\tau_{\mathrm{SXR}} = (43 \pm 1)$ as, a new world record, generated from a two-cycle pulse with a pulse duration of $\tau_{\mathrm{IR}} = (11.1 \pm 0.7)$ fs pulse duration.

In section 4.2, we have used the method described above to study partially angle-integrated streaking-spectrograms as obtained from MB-TOF spectrometers, where a complete and accurate reconstruction of attosecond pulses for large collection angles (MB-TOF, VMI) has not been demonstrated so far. Using a numerical angle-integrated streaking spectrogram, we performed the retrieval using the new developed ML-VTGPA including photoelectron angular distribution, fully accounting for the angle-dependent complex amplitude describing the transition from the ground state to the continuum. The dependence of the reconstruction on the collection angle has been analyzed. Already, after a few iterations of the algorithm the acceptance angle can be judged by the MSE that decreases fastest for close to the input maximum collection angle. This also gives an experimental measure of the collection angle of the MB-TOF used. For a reasonably well selected acceptance angle, the obtained pulse parameters are well extracted by the ML-VTGPA including PAD. For the case of a $\tau_{\mathrm{SXR}} = 350$ as SXR pulse and $\tau_{\mathrm{IR}} = 3.5$ fs IR pulse, we show that for a tolerance of $\Delta\theta_{\mathrm{max}} = \pm 10^{\circ}$ in the angle-integration, the retrieved pulse durations show approximately an error of ±5%. In conclusion, we have demonstrated the accurate and complete characterization of attosecond pulses lasting less than one atomic unit of time and covering X-ray absorption edges of most light elements and the streaking IR field using the ML-VTGPA including PAD.

With further advances in laser technology, laser-based HHG sources will reach soon even higher photon energies with reasonable flux and will provide broadband supercontinua up to the keV-region. For a complete and reliable pulse characterization, the ML-VTGPA including photelectron angular distribution is ideally suited, as it incorporates the physics of the electron wave packet generated from the SXR pulse and allows to mitigate the low photon flux from mid- or long-wavelength driving lasers, by including the integration over a large polar angle. This paves the way to trace ultrafast charge migration with almost any sample by attosecond transient absorption at the K-edges of carbon (284 eV), nitrogen (401 eV), and oxygen (533 eV). Reaching the L-edges titanium (455 eV), vanadium (513 eV), chromium (575 eV), iron (710 eV), cobalt

Optics EXPRESS

(779 eV), nickel (855 eV), and copper (955 eV) will allow the study of time-resolved phenomena of the 3d transition metals by using well known techniques like time-resolved X-ray absorption spectroscopy (XAS), X-ray absorption near-edge spectroscopy (NEXAFS, XANES), and X-ray emission spectroscopy (XES) with atto- to femto-second time resolution.

Funding

ERC Starting Grant (contract 307270-ATTOSCOPE); NCCR-MUST, a funding instrument of the Swiss National Science Foundation; SNF (200021_159875).

Acknowledgment

T.G. and A.J. contributed equally to this work. We thank Aaron von Conta for performing SFA calculations that highlighted the role of angular integration in streaking spectrograms.